

The Air Flow Distributions within a Typical Planar Protonic Ceramic Fuel Cell Stack

M. Zhu¹, Z. Yang¹, Z. Han¹, A. Ishutkin², A. Raza¹, Z. Yu^{1,*}, D. Chen^{1,*}

¹ School of Energy and Power, Jiangsu University of Science and Technology, Zhenjiang 212100, China

² National Research Ogarev Mordovia State University, Saransk 430005, Russia

*E-mail: dfchen01@163.com

Received: 2 March 2022 / Accepted: 12 April 2022 / Published: 7 May 2022

With the in-depth research of solid oxide fuel cell (SOFC), the advantages of the protonic ceramic fuel cell (PCFC) have been paid more and more attentions. In this paper, three-dimensional calculated fluid dynamics model was built to investigate the fluidity within a typical PCFC stack. The result shown that for a typical PCFC stack, the air mass flow rate fed to the piled layers would keep decreasing with the increasing cell number index, while the inlet and outlet manifolds had similar cross section areas. Extending the length of the membrane electrode assemblies (MEA) would slightly improve the air flow distribution uniformity. The air flow and species distributions among the rib channels would be determined by the sites of the entrances and exits of the manifolds. and the solid rib configuration over porous cathodes. The vapor mole fraction distribution over the dense electrolyte surface had apparently oppositely with the rib channel configuration, because two mole vapors were generated while one mole oxygen is consumed. Different from the O-SOFC stack, the vapor removing capacity would be an important factor for evaluating the quality of the cathode side flow path structure.

Keywords: Protonic ceramic fuel cell stack; Rib channels, 3D calculated fluid dynamics model, Vapor removing capacity.

1. INTRODUCTION

With energy conservation and emission reduction becoming a focus of today's society, the efficient and clean use of natural resources has been paid more and more attentions by researchers all over the world. Solid oxide fuel cell (SOFC) has the advantages of high efficiency, wide range of fuel selection and environmental protection, which has been widely concerned because of suitable for the current industrial power generation [1]. SOFC can be divided into oxygen-ion conduction type (O-SOFC) and proton conduction type (H-SOFC) according to the ion transferred by the ceramic electrolyte [2]. Among them, H-SOFC with protonic ceramic conductor as electrolyte is a very promising power

generation device [3, 4]. Electrolyte of O-SOFC is based on oxide that can conduct oxygen ion (such as YSZ), and its application in medium temperatures is restricted because of the high migration activation energy of oxygen-ions [5, 6]. Different from O-SOFC, which generates vapor in anode, H-SOFC generates vapor in cathode side without diluting the fuel at the anode side, which improves fuel efficiency [7]. At present, research about H-SOFC mainly focuses on protonic ceramic fuel cell (PCFC). The properties of the proton-conducting ceramic electrolyte enable the PCFC to operate at intermediate temperatures (350-650°C) [8]. In addition, PCFC provides a higher operating voltage than the conventional O-SOFC because it does not dilute the fuel in the anode [9]. Compared with other type fuel cells, these advantages give PCFC a certain concern [10, 11].

The research on PCFC has never stopped since people pay attention to it. At present, the research on PCFC mainly focuses on the preparation of electrolyte, cathode, and anode grade materials. Duan [12-14] found in their study that the poor performance of most PCFCs were partly due to the cathodes materials. Thus, a perovskite-type cathode combination specifically designed for PCFC was developed and tested by five different PCFC button cells. Duan also reported a total of 11 different fuels, including hydrogen and methane, to conduct long-term tests and obtain performance data on PCFCs. Most of them were proved to had both excellent performance and excellent durability. Recently, experimental results on the effect of gas humidification on PCFC performance were reviewed in Ref. [15]. In additional to the novel material exploring, three-dimensional (3D) calculating fluid dynamic (CFD) modeling was also very important to a identify the working processes within PCFC stack and improve the stack performance. The modeling of O-SOFC and protonic exchanger membrane fuel cell (PEMFC) stacks had been widely reported [16, 17]. General problems and the latest PCFC modeling are reviewed in [18, 19]. PCFC models can be distinguished based on the following aspects: operation mode, fuel cell geometry, equipment complexity, fuel, and so on.

At present, most theoretical studies focus on fluid mass transfer [20], porous electrode [21] and electrolyte properties [22], heat transfer and electrode polarization mechanism [23]. J. Milewski [24] created a PCFC model with Aspen Hysys software with only 0.01 V error from the actual work. In the past decades, most 3D CFD models were established for the O-SOFC stack, there were a few simulations about the flow structure of PCFC stacks. Chen [25] established a set of 3D large-scale 3D CFD models, which were built to optimize the flow paths of air/fuel in the O-SOFC stacks. They calculated the minimum flow rate, pressure drop and standard mass flow rate per cell to characterize the distribution effect of air and fuel within the flow paths of O-SOFC stacks. Recently, the 3D CFD model of the typical PCFC stacks was developed to investigate the effects of the manifold cross section areas [26] and rib channel configurations [27] on the flow distributing qualities.

In this paper, 3D models for three PCFC stacks with similar structures are built in order to study the effect of the length to width ratios of membrane electrode assembly on the fluidity of PCFC stacks. At the same time, the air flow distribution of several characteristic cells in PCFC stack and the influence of length of feed/exhaust header on the air flow in cell gas channel over the cathode are investigated. The research results will provide great experience for the simulation of subsequent multi-physical fields of PCFC stacks.

2. STACK STRUCTURE AND CFD MODEL

In **Fig. 1**, a typical planar stack with three inlets and outlets [28] is adopted to establish and discuss the working process within a typical 25-cells PCFC stack. The complete stack consists of several repeating units connected in series. Each unit is mainly composed of metal frames, bipolar plates, membrane electrode assemblies (MEA) and seals [29, 30]. The bipolar plate acts for connecting the fuel cells in series, collecting the produced electric current, and uniformly distributing the flows. The solid ribs are connected on both sides of the bipolar plate to evenly collect electric currents from the cathode and anode surfaces, respectively. The rib channels constructed by the solid ribs will spread the air flow over the cathode surface uniformly and collect the cathodic producing vapor. Membrane electrode assembly (MEA) includes the anode support layer, anode function layer, electrolyte, cathode support layer, and cathode function layer. Seals are applied between the interconnect and the electrodes in order to insulate fluid domain. Inside the solid structure of the stack, there are fluid areas for air and fuel transfer as shown.

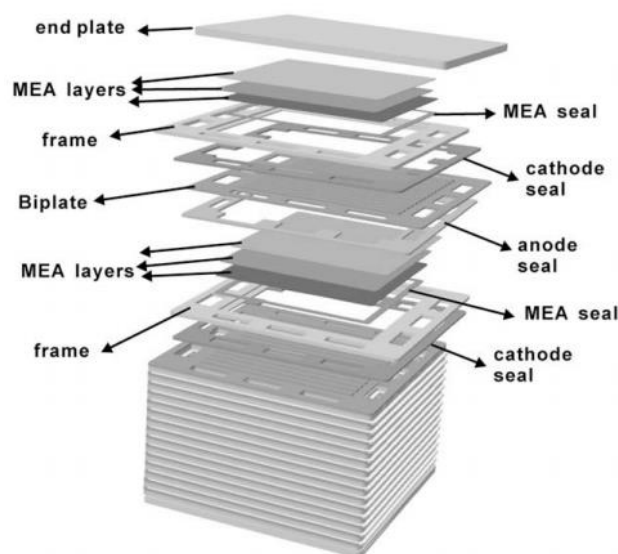


Figure 1. The structure of a typical fuel cell stack structure with three inlets and outlets [28].

Fig. 2 further displays the complete fluid domain structure referring to the cathode side of the 25-PCFCs stack corresponding to the design in **Fig. 1**. The entire cathode side stack model includes, three inlet and outlet manifolds, flow channels over cathode surface, cathode collecting layers, and cathode functional layers. The flow field over each cathode collecting layer surface consists of three parts: three entrances, three exits and 17 gas rib channels connected in parallel. Three entrances for each cell are part of the stack inlet manifolds, which lead the air into the PCFC unit and transport the excess to the next cell. Outlet manifold is responsible for collecting the excess air and products and transferring them to the outlet. The cell gas channels are attached to the cathode collecting layer. Gas is evenly distributed on surface of the electrode through rib channels. Air is piped from the bottom of the inlet manifold into each layer cell gas channel, which is distributed in each unit of the cathode surface afterwards. Then, the excess gas enters the outlet manifold with the generated water and is discharged from the outlet. The entrances of the inlet manifolds are on the same side as the exits of the outlet

manifolds, which lead to the flow path configuring in a U-shape. The rib channels over the cathode surface are perpendicular to each other.

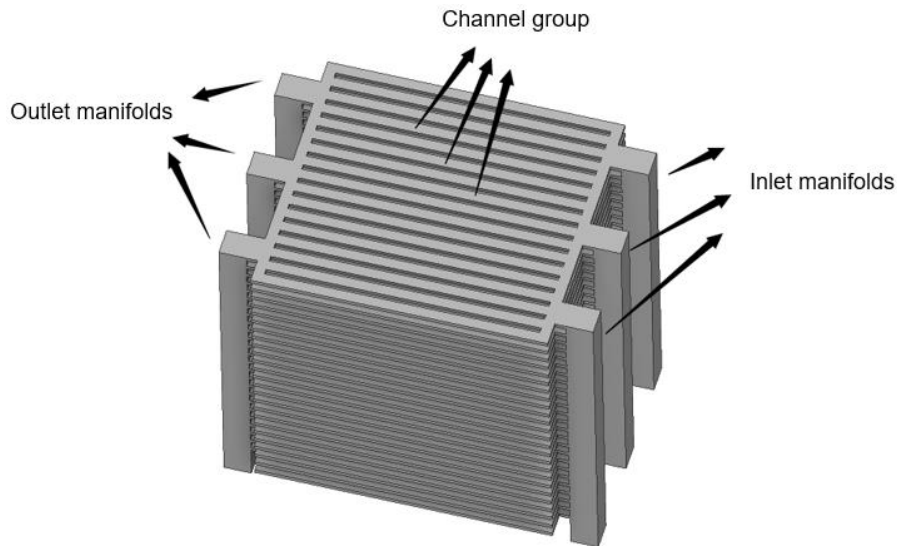


Figure 2. 3D CFD model for the cathode side gas path within a 25-PCFCs stack.

Table 1. Geometry parameters for the 25-cells PCFC stack.

Component	Air side	Fuel side
Channel dimension (width × height):	4 × 1.5 mm ²	4 × 1.5 mm ²
Rib dimension (width × height):	2 × 1.5 mm ²	2 × 1.5 mm ²
Feeding header (length × width):	5 × 100 mm ²	5 × 100 mm ²
Combining header (length × width):	5 × 100 mm ²	5 × 100 mm ²
MEA area (Stack A) (length × width × height)	100 × 100 × 0.6 mm ³	100 × 100 × 0.6 mm ³
MEA area (Stack B) (length × width × height)	150 × 100 × 0.6 mm ³	150 × 100 × 0.6 mm ³
MEA area (Stack C) (length × width × height)	100 × 150 × 0.6 mm ³	100 × 150 × 0.6 mm ³
Height of a single cell	4.5 mm	4.5 mm
Inlet manifold (length × width):	10.0 × 10.0 mm ²	10.0 × 10.0 mm ²
Outlet manifold (length × width):	10.0 × 10.0 mm ²	10.0 × 10.0 mm ²

We can take advantage of the Navier-Stokes equation combined with the continuity equation to simulate momentum transfer within the gas path of PCFC stack as:

$$\nabla \cdot (\rho \bar{u} \bar{u}) = \rho \bar{f} - \nabla p + \frac{1}{3} \mu \nabla (\nabla \cdot \bar{u}) + \mu \Delta \bar{u} \quad (1)$$

$$\nabla \cdot (\rho \bar{u}) = 0 \quad (2)$$

where ρ is the density of the fluid, \bar{u} is the vector of the velocity, p is the pressure of the fluid, \bar{f} is the mass force per unit mass, μ is the dynamic viscosity that based on the ideal gas mixing law.

Species conservation equation can is shown as follow:

$$\nabla \cdot (\varepsilon \rho Y_\alpha \bar{u}) = \nabla \cdot (\rho D_{\alpha, \text{eff}} \nabla Y_\alpha) + S_\alpha \quad (3)$$

where, ε is the porosity of the porous electrode, $D_{\alpha, \text{eff}}$ is the effective gas diffusion coefficient, Y_α is the mass fraction of species α . S_α is the source item that exists in the cathode functional layers.

For the other dominations except for the cathode functional layers, $S_{\alpha}=0$. For the cathode functional layers, however, they can be expressed by the following formulas:

$$S_{O_2} = -i \frac{M_{O_2}}{4Fl}, S_{H_2O} = i \frac{M_{H_2O}}{2Fl}, S_{N_2} = 0 \quad (4)$$

where i is the average current density. M_{α} is the molar mass. F is Faraday constant. l is the thickness of the cathode functional layer.

The air inlet velocity can be derived by the following formula:

$$u_{air}^{in} = \frac{NiAM_{air}}{4\eta_{O_2}\chi_{O_2}\rho_{air}A_{air}} \quad (5)$$

where N is the layer number of the PCFC stack, A is the effective reaction area of a single cell, M_{air} is the molar mass of air, η_{O_2} is the utilization rate of air flow on stack level, χ_{O_2} is the mole fraction of oxygen within the input air flow, ρ_{air} is the density of the air flow, and A_{air} is the total cross sectional area of the stack entrances.

The K-Epsilon turbulence model is built for our calculations. Velocity inlet and pressure outlet are set up for boundary conditions while the rest of the boundaries are adiabatic. In order to ensure the appropriate utilization rate of oxygen, the inlet velocity is determined by the number of PCFC units within the stack, the average current density, and the area of the MEA [31]. The parameter Settings for the remaining boundary conditions are listed in **table 2**.

Table 2. Parameters and conditions for the 3D CFD model

Parameters	Values
Pressure	101325 Pa
Air inlet temperature	823 K
Oxidizer mole fraction at inlet	21% O ₂ , 79% N ₂
Velocity at the oxidizer inlet	14.46, 21.69 (m s ⁻¹)
Number of main inlet pipes	3
Average current density	5000 (Am ⁻²)
S_{O_2}	-41.5 (kg/m ³ s)
S_{H_2O}	46.6 (kg/m ³ s)

In order to compare the qualities of the flow distribution among the piled PCFCs, over each PCFC unit and within the porous cathodes in an more convenient way, here we use two evaluation indexes: the minimum air flow rate and the normalized air mass flow rate.

We use Γ_L index for the minimum flow rate obtained by the piled PCFC units to indicate the air flow distributing qualities among the piled PCFC units [25]. High value of Γ_L indicates that the uniformity of flow distribution in PCFC stack is better, otherwise the flow distribution in the stack is poor.

$$\Gamma_L = \min(\dot{m}_{L,1} : \dot{m}_{L,N}) \quad (6)$$

where $\dot{m}_{L,i}$ represents the normalized air mass flow rate of a PCFC unit in the i -layer of the stack, which can be calculated by the following formula:

$$\dot{m}_{L,i} = \frac{m_{L,i}}{ave(m_{L,1} : m_{L,N})} \tag{7}$$

In the formula above, $m_{L,i}$ represents the mass flow rate fed to the PCFC layer i .

3. RESULT AND DISCUSSION

Fig. 3 shows three 25-cells stacks with different ratios of length to width of the MEA area. Stack A has a ratio of length to width 1:1. Stacks B and C have the same MEA areas but different ratios of length to width, 1.5:1 and 1:1.5, respectively. Different proportions of MEA areas change the proportions of corresponding cell gas channels. Among them, for the width of stack C changes from 100 mm to 150 mm, the number of air rib channels increases from 17 to 25. While the three stacks have similar structure, there are no different with the sizes of each air channel of them.

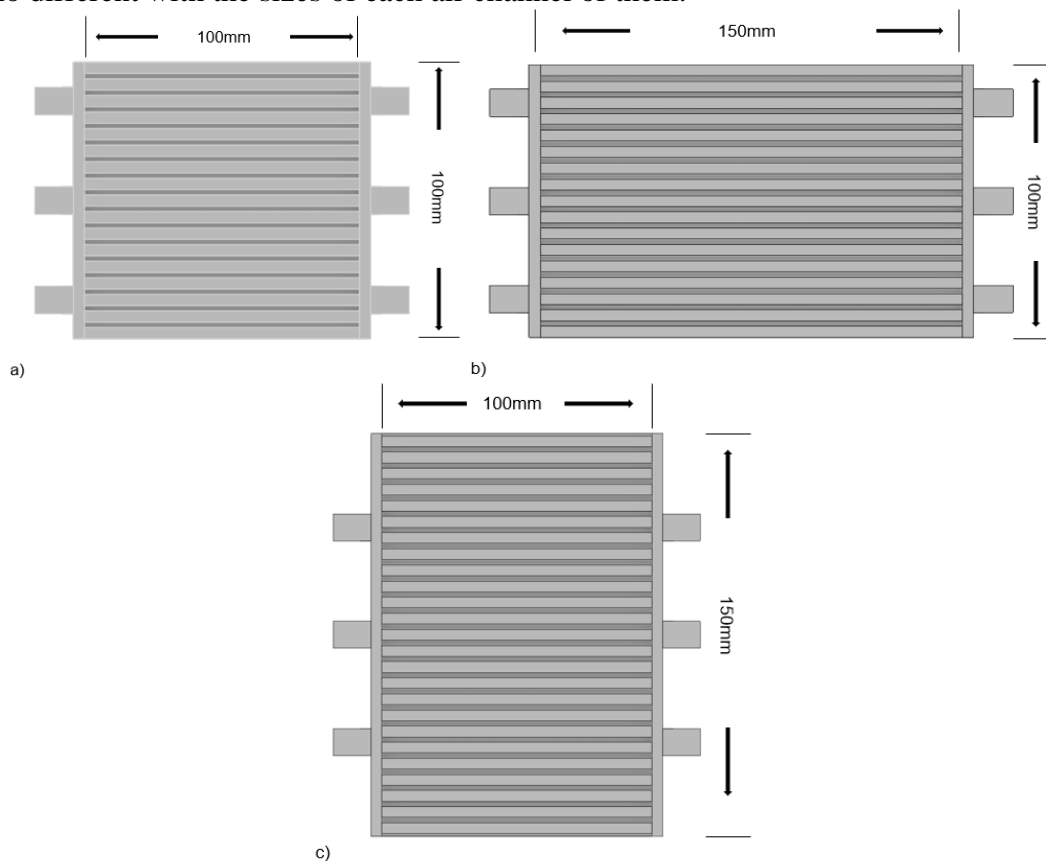


Figure 3. a) Ratio of length to width of stack A 1:1; b) Ratio of length to width of stack B 1.5:1; c) Ratio of length to width of stack C 1:1.5.

Fig. 4 compares the distributions of the corresponding normalized air mass flow rate of PCFC units among the three different stacks. The cell nearest the stack entrance is defined as 1-st. The number index is increased as the distance between cell unit and stack entrance increased. Firstly, for stacks A, B and C, the normalized air mass flow rate of each layer gradually decreases, while the PCFC unit index

is increased. These results are similar with that of the traditional O-SOFC stacks [32] and PEMFC stacks [16]. We can get that for both the PCFC and O-SOFC stacks, the air mass flow rate of the piled layer will keep decreasing with the increasing cell number, while the inlet and outlet manifolds adopt the same cross section areas.

It can be inferred that the stack B has the best stack uniformity with a minimum flow rate index $\Gamma_L = 0.68$, while the stack C has the worst air flow feeding quality $\Gamma_L = 0.54$. It means that increasing the flow resistance over the electrode surface will increase the flow distributing uniformity among the piled layers. Thus, changing the structure parameters of a PCFC stack will affect the air flow distributions. Extending the length of the MEA will slightly improve the air flow distribution uniformity among the piled PCFC units. Extending the width of the MEA, however, will decrease the air flow distribution uniformity among the piled PCFC units, which may lead to inadequate electrochemical reaction in some regions. This conclusion is consistent with the result obtained by [26] basing on the different PCFC stack design.

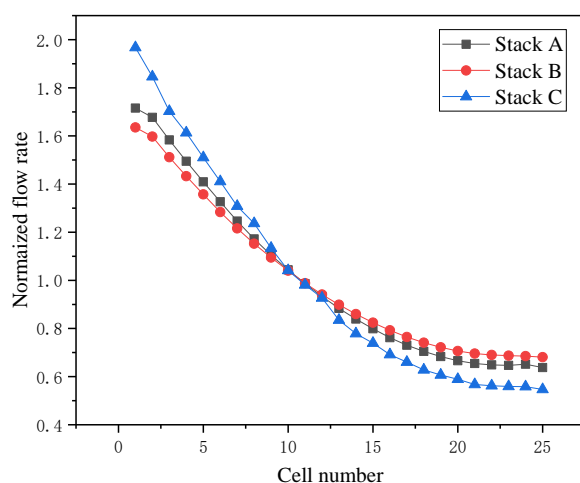


Figure 4. Corresponding distributions of the normalized air mass flow rate fed to the piled PCFC units of stacks A, B and C, respectively.

Taking the 1-st and 25-th PCFC units as examples, **Fig. 5a** and **5b** further compares the normalized air mass flow rate distributions among the rib channels of stacks A, B and C. The stack A and stack B both have 17 rib channels, while the stack C has 25 rib channels. As shown in **Fig. 5a**, the rib channels near the three entrances (or three exits) of the inlet manifold will receive most of the air flow. The distribution of the normalized flow rate among the rib channels has three peaks. Thus, we can get that the position of the entrance and exit will be the key factor to lead the air flowing. This conclusion can be further supported by the calculated result in our previous paper [27], which is a 3D CFD model basing on the different structure design of PCFC stack. Compared the air flow distributions over the cathode surfaces of 1-st and 25-the PCFC units in **Figs. 5a** and **b**, we can get that the rib channels of stack B has the best normalized flow rate distributing quality. stack C has the worst normalized flow rate distribution quality among the rib channels, compared with the other two stacks. While the feed/exhaust

header length is increased from 100 to 150 mm, the number of rib channels is increased and the slope of the air flow distribution line is increased.

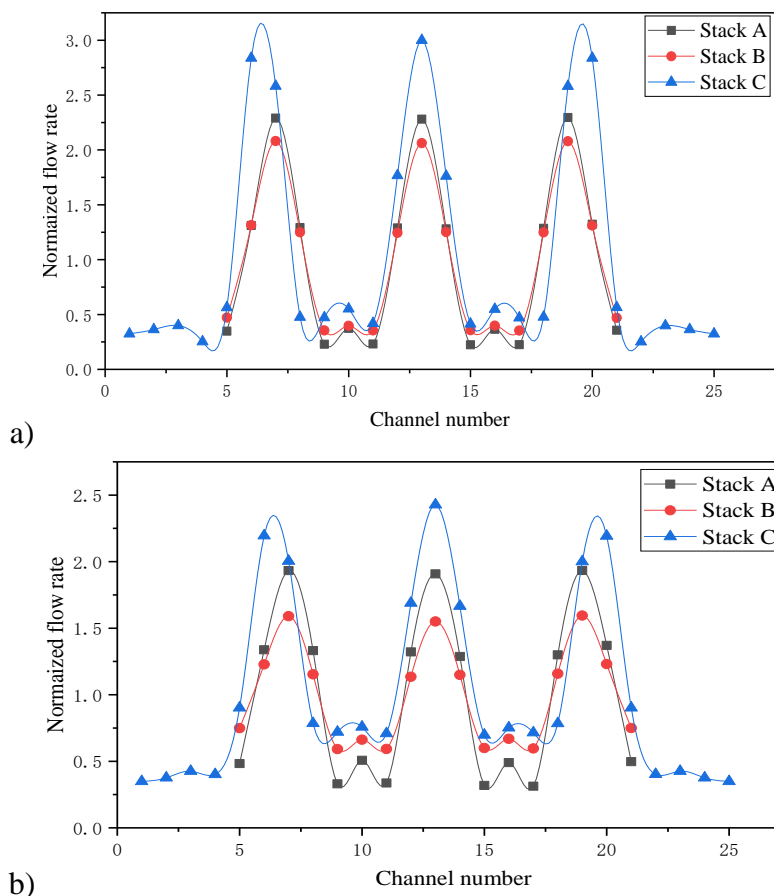


Figure 5. Normalized flow rate distributions over: a) the 1-st PCFC unit.; b) the 25-th PCFC unit.

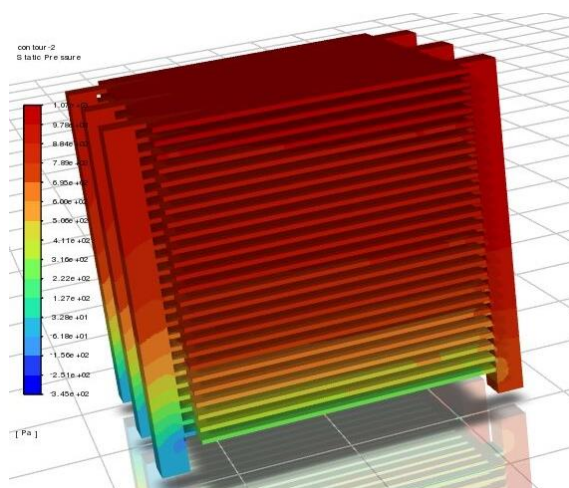


Figure 6. The static pressure distribution within the PCFC stack.

Obviously, from **Fig. 4** we can get that the uniformity of the air flow rate of PCFC stack is relative smaller than that of O-SOFC stack [28]. Because two moles vapor are generated within the cathode

functional layer of PCFC stack, instead of the anode functional layer of the O-SOFC stack, while one mole of oxygen is consumed within the cathode side. Taking stack A as an example, the static pressure distribution within the PCFC stack is displayed in **Fig. 6**. Similar with the O-SOFC stack [28], for the inlet manifold of PCFC stack, the pressure will increase gradually as the distance between position and stack entrances is increased. On the outlet manifold side, however, the pressure will decrease gradually as the distance between position and exit is decreased. The decreasing slope is bigger than that of O-SOFC with the same structure [28], because the vapor is generated in the cathode side of PCFC stack instead of the anode side of O-SOFC stack.

Fig. 7a further shows the mole fraction distribution of oxygen within the PCFC stack and over the dense electrolyte surface of 1-st PCFC unit. Obviously, the species distributions are greatly affected by the solid rib geometric configuration. Firstly, the air flow and oxygen are concentrated to those rib channels near the three entrances of the inlet manifold. Secondly, the oxygen mole fraction distribution over the dense electrolyte has similar configuration with the rib channel configuration constructed by the solid ribs. Obviously, although the air flow is mostly fed to the 1-st PCFC unit, the oxygen diffusion from the rib channels to those areas covered by the solid ribs is still difficult.

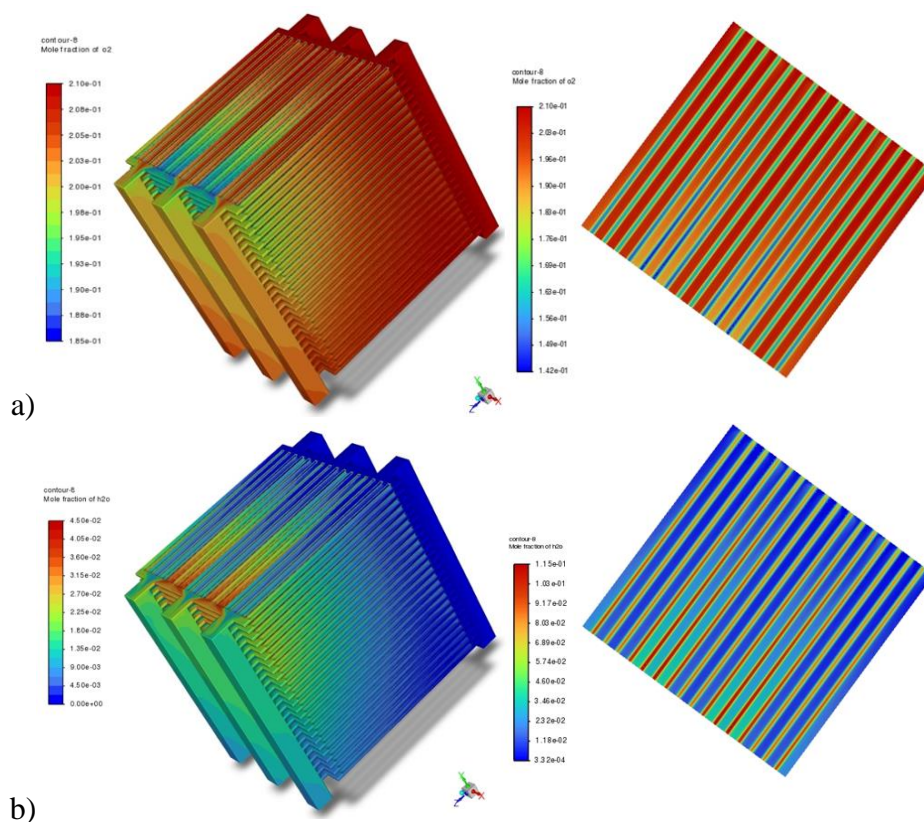


Figure 7. The species mole fraction distribution within the PCFC stack and over the dense electrolyte surface of 1st PCFC unit: a) Oxygen, b) Vapor.

Nitrogen is not consumed or generated during the PCFC working processes. The vapor mole fraction distribution within the PCFC stack and over the dense electrolyte surface have apparently oppositely with that of oxygen distributions. Two moles vapor will be generated, while one mole of

oxygen is consumed over the electrolyte surface. The regions covered by the rib channels have smaller vapor mole fraction than those zones covered by the solid ribs, because of the high water removing capacity. Those areas covered by the solid ribs, however, have very low vapor removing capacities and should be further improved by structure optimization.

In Fig. 8, the normalized distributions of the air mass flow rates among the piled PCFC units of stack A are compared, while the cross section areas of the manifolds are extended from 10 mm×10 mm to 10 mm×20 mm. The uniformity of the air flow feeding rates among the piled PCFC units will be greatly improved, while the cross section area of the manifold is enlarged. The corresponding stack uniformity index of the stack A will be raised from 0.64 to 0.77. This result is consistent with the that obtained from O-SOFC stacks [28].

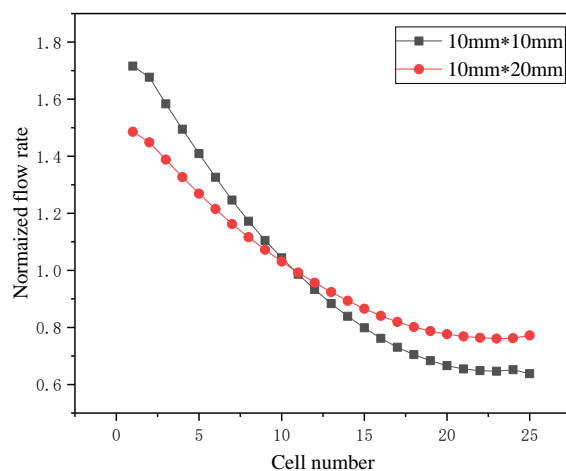


Figure 8. Dependence of the distributions of the normalized air mass flow rate fed to the piled PCFC units on the cross-sectional area of manifolds.

4. CONCLUSION

3D CFD models for 25-PCFCs stack have been established to study the effect of different geometric parameters on the air flow and species distributions characteristics within a PCFC stack and the following conclusions are obtained:

i) Similar with the traditional O-SOFC stack, the air mass flow rate of the piled layer of a typical PCFC stack will keep decreasing with the increasing cell number, while the inlet and outlet manifolds adopt the same cross section areas.

ii) Extending the length of the MEA will slightly improve the uniformity of air flow distribution among the PCFC cells. Extending the width of the MEA, however, will decrease the air flow distribution uniformity among the piled PCFC cells.

iii) The distribution of the flow rate among the rib channels has three peaks in current PCFC stack design. The position of the entrance and exit will be the key factor to lead the air flowing distribution over the porous cathode surface.

iv) The uniformity of the air flow rate of PCFC stack is relative smaller than that of O-SOFC stack with the same structures. Because two moles vapor are generated within the cathode functional layer of PCFC stack, instead of the anode functional layer of the O-SOFC stack, while one mole of oxygen is consumed within the cathode side.

v) Those areas covered by the solid ribs have low vapor removing capacities and should be further improved by optimizing the configuration of the solid ribs of the PCFC stack.

ACKNOWLEDGEMENTS

This research was funded by the financial support of the Ministry of Science and Technology of the People's Republic of China (CU03-10) and Jiangsu Education Department (1154702001-1).

References

1. S.P. Jiang, *Int. J. Hydrogen Energy*, 44 (2019) 7448.
2. C.Y. Gu, X.S. Wu, J.F. Cao, J. Hou, L. N. Miao, Y.P. Xia, F. Chao and W. Liu, *Int. J. Hydrogen Energy*, 45 (2020) 23422.
3. B. Hua, N. Yan, M. Li, Y.F. Sun, Y.Q. Zhang, J. Li, T. Etsell, P. Sarkar and J.L. Luo, *Adv. Mater.*, 28 (2016) 8922.
4. K. Ding, M. Zhu, Z. Han, V. Kochetov, L. Lu and D. Chen, *Ionics*, 26 (2020) 4567.
5. M. Rashid, A. Samat, A. Jais, M. Somalu, A. Muchtar, N. Baharuddin and W. Isahak, *Ceram. Int.*, 45 (2019) 6605.
6. Y.B. Zhang and J.D. Nicholas, *J. Electrochem. Soc.*, 168 (2021) 034513.
7. H.Y. Zhu, R.J. Braun and R.J. Kee, *J. Electrochem. Soc.*, 165 (2018) F942.
8. D.Y. Hu, J. Kim, H.J. Niu, L.M. Daniels, T.D. Manning, R.Y. Chen, B.W. Liu, R. Feetham, J.B. Claridge and M.J. Rosseinsky, *J. Mater. Chem. A*, 10 (2022) 2559.
9. F. Calise, G. Ferruzzi and L. Vanoli, *Appl. Energy*, 86 (2009) 2401.
10. D. Hu, J. Kim, H. Niu, L.M. Daniels, T.D. Manning, R. Chen, B. Liu, R. Feetham, J. Claridge and M.J. Rosseinsky, *J. Mater. Chem. A*, 10 (2022) 2559.
11. J. Wang, Z. Li, H. Zang, Y. Sun, Y. Zhao, Z. Wang, Z. Zhu, Z. Wei and Q. Zheng, *Int. J. Hydrogen Energy*, 47 (2022) 9395.
12. C. Duan, J. Tong, M. Shang, S. Nikodemski, M. Sanders, S. Ricote, A. Almansoori and R. O'Hayre, *Science*, 349 (2015) 1321.
13. C. Duan, R. Kee, H. Zhu, N. Sullivan, L. Zhu, L. Bian, D. Jennings and R. O'Hayre, *Nat. Energy*, 4 (2019) 230.
14. C. Duan, R. Kee, H. Zhu, C. Karakaya, Y. Chen, S. Ricote, A. Jarry, E.J. Crumlin, D. Hook, R. Braun, N.P. Sullivan and R. O'Hayre, *Nature*, 557 (2018) 217.
15. M. Santin, A. Traverso and L. Magistri, *Appl. Energy*, 86 (2009) 2204.
16. D. Chen, Y. Zou, W. Shi, S. Serbin and H. You, *Int. J. Energy Res.*, 45 (2021) 9948.
17. D. Chen, K. Ding, Z. Chen, T. Wei and K. Liu, *Energy Convers. Manage.*, 178 (2018) 190.
18. Z. Li, Q. He, L. Xia, Q. Xu, C. Cheng, J. Wang and M. Ni, *Int. J. Hydrogen Energy*, 47 (2022) 4047.
19. K. Li, T. Araki, T. Kawamura, A. Ota and Y. Okuyama, *Int. J. Hydrogen Energy*, 45 (2020) 34139.
20. J.Q. Dai, Z. M. Yang, W.S. Wang, J. P. Liu, Y.D. Akenteng and D.F. Chen, *Ionics*, 28 (2022) 1863.
21. A. Seong, J. Kim, J. Kim, S. Kim, S. Sengodan, J. Shin and G. Kim, *J. Electrochem. Soc.*, 165 (2018) F1098.
22. J. Lyagaeva, N. Danilov, A. Tarutin, G. Vdovin, D. Medvedev, A. Demin and P. Tsiakaras, *Dalton*

Trans., 47 (2018) 8149.

23. Y. Kawabata, T. Nakajima, K. Nakamura, T. Hatae, Y. Tachikawa, S. Taniguchi, Y. Matsuzaki and K. Sasaki, *J. Power Sources*, 448 (2020) 227459.
24. J. Milewski, A. Szczesniak and L. Szablowski, *J. Power Sources*, 502 (2021) 229948.
25. D.F. Chen, Z.Y. Chen, J. Li, J.Q. Zhang and K. Liu, *Int. J. Electrochem. Sci.*, 14 (2019) 2857.
26. J.Q. Dai, M.F. Zhu, H.Z. Zhang, J.P. Liu and D.F. Chen, *Int. J. Electrochem. Sci.*, 16 (2021) 211052.
27. J. Dai, D. Uwaneza, A. Levtshev, Z. Yu and D. Chen, *Int. J. Electrochem. Sci.*, 17 (2022) 220116.
28. W. Bi, D. Chen and Z. Lin, *Int. J. Hydrogen Energy*, 34 (2009) 3873
29. M.A. Khaleel, Z. Lin, P. Singh, W. Surdoval and D. Collin, *J. Power Sources*, 130 (2004) 136.
30. Z. Lin, J.W. Stevenson and M.A. Khaleel, *J. Power Sources*, 117 (2003) 92.
31. S. Su, H. He, D. Chen, W. Zhu, Y. Wu, W. Kong and B. Wang, L. Lu, *Int. J. Hydrogen Energy*, 40 (2015) 577.
32. D. Chen, Y. Xu, M. O. Tade and Z. Shao, *ACS Energy Lett.*, 2 (2017) 319.

© 2022 The Authors. Published by ESG (www.electrochemsci.org). This article is an open access article distributed under the terms and conditions of the Creative Commons Attribution license (<http://creativecommons.org/licenses/by/4.0/>).